SUPPLEMENTARY INFORMATION

1 Supplementary methods

1.1 Optical setup

We carry out our experiments in a home-built cryogenic confocal setup. Our bulk diamond sample, a natural type IIb diamond of high purity, is kept below 7 K in a Janis ST-500 Cryostat. Optical access to individual NV centers is facilitated with a Nikon 0.95 NA Plan-Apo microscope objective that is held inside vacuum with a bellow structure that allows the objective to be moved relative to the sample. Our microscope contains two excitation channels and two collection channels. The NV is off-resonantly excited and spin polarized using a doubled YAG laser (532 nm Coherent Compass 315M-100) modulated with an acousto-optical modulator (Isomet 1250C-848). Resonant optical pumping is carried out with two external cavity grating lasers. A New Focus Velocity TLB 6304 laser operating at 637.199 nm and locked to a Fabry-Perot cavity (Atrix Management S A CC - 3.0GHz - 200) is used for the readout transitions ($\sim 4\ \mu$W before objective), while a second laser (Atrix Management S A ECLD-0638-022) operating at 637.189 nm is used for resonant optical pumping of the entanglement generation transition ($\sim 100\ \mu$W before objective). Both lasers are modulated with acousto-optical modulators (Crystal Tech 3080-122). In addition, a high fidelity excitation pulse (2 ns 3dB width and > 50 dB extinction in 4 ns from peak) is generated from the 637.189 nm laser using two waveguide modulators in cascade (Guided Color Technologies), each controlled by an 800 MHz arbitrary waveform generator (Analogic Polynomial Waveform Synthesizer 2045). Extinction of the excitation pulse is critical because we use the relatively long lifetime of the NV center to seperate the emission from the shorter (2ns) laser reflection photons.

Phonon-sideband emission from the NV is separated by dichroic filters from the 532 nm excitation path (Semrock LPD01-532RS-25) and ZPL path (Semrock Di01-R635-25x35) before being filtered to remove any leakage or dominant raman lines (2x Semrock NF01-633U-25, Semrock LP01-633RS-25). It is then coupled into a single mode fiber and sent to a high quantum efficiency APD (SPCM ARQ-15-FC). The ZPL collection path is separated from the resonant excitation path by a non-polarizing beam splitter, and emission from the NV is sent to a polarization analysis setup consisting of a HWP and a PBS. The emission is filtered by two narrow frequency filters (custom Andover 1 nm bandpass around 638 nm, Semrock FF01-640/14-25) and detected by a low-dark count APD (Micro-Photon-Devices, PDM Series). We use a third waveguide based E-O modulator (EOSpace, driven by Stanford Research Systems DG645 delay generator) before the detector to reduce the number of reflected photons from the excitation pulse and suppress afterpulsing of the detector.

1.2 Microwave control

The two microwave transitions are addressed individually by separate oscillators: a HP 8350B sweep oscillator with 83525A RF plugin tuned to 2.9387 GHz and an Agilent 83732B synthesizer tuned to 2.8174 GHz. For simultaneous addressing, a 60.85 MHz waveform generated by a high speed Tek 710 AWG is mixed using a Minicircuits ZFM-15 mixer with the RF field generated from the Agilent synthesizer at 2.87875 GHz. To balance the power of the two microwave frequencies of the simultaneous field, they are first separated using two bandpass filters with 120 MHz bandwidth around 2.8 GHz and 3.0 GHz (Reactel 5C7-2800-120S11 and

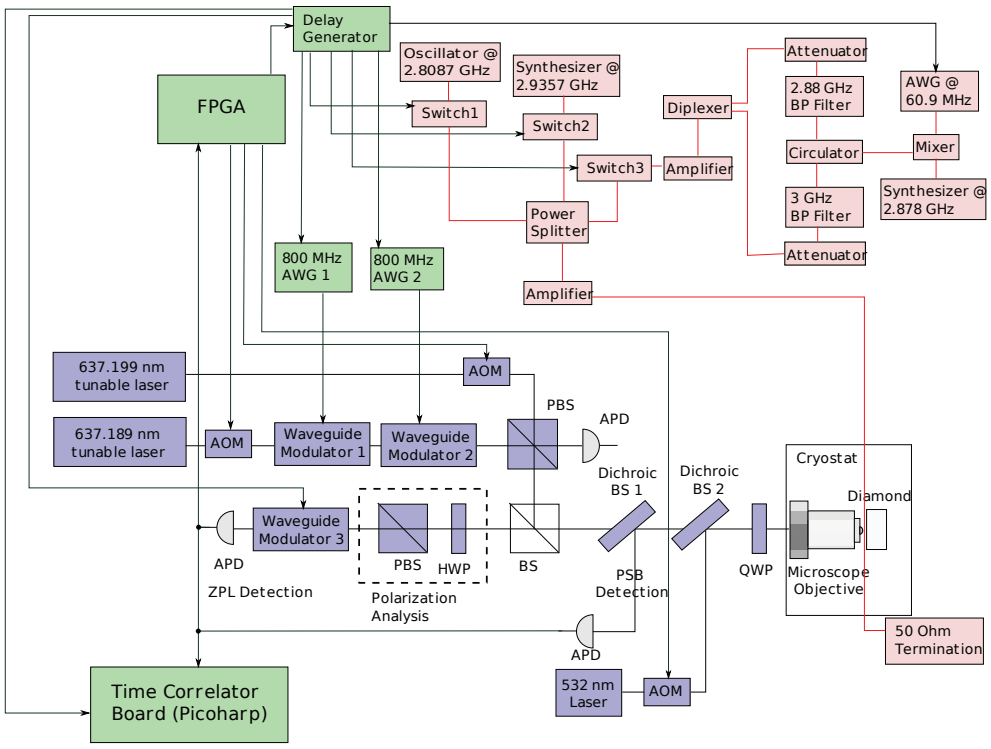

Figure S1: **Experimental Setup.** The setup is shown in three functional groups. The optical setup is show in blue and gray. In green are the control electronics and the electrical pulses that are generated. A green arrowed line indicates a pulse being generated by the source device and sent to the entity indicated by the arrow. For example the FPGA generates the pulse that drives the AOM for 637.199 nm readout laser. The microwave components and their connections are shown in red.

5C7-3000-120S11). They are then recombined using a diplexer around the same frequencies (Reactel 2DP7-2800/3000-X120S11) after being individually attenuated (Minicircuits ZX76-15R5-PP-S+) and re-amplified (Minicircuits ZX-60-6013E+). The measured variance in the relative phase between two frequencies of the simultaneous field is below 0.19 radians. Fast microwave switches (Minicircuits ZASWA-2-50DR+, Custom Microwave Components S0947A-C2) are used for time shaping of microwave pulses. All separate channels are combined and sent to a 10 W solid state amplifier (Ophir 530324-002) before the copper wire.

1.3 Experiment control and data acquisition

Experimental flow is controlled by a NI-7833R FPGA based intelligent DAQ device programmed to run the entanglement generation sequence and switch to the readout sequence within three clock cycles (75ns) upon the detection of a ZPL photon. Time of arrival information of photons on both PSB and ZPL channels are collected by passively combining the output of the two APDs to the input of a time-tagged-single-photon-counting device (Picoharp 300). The device is configured to record the time of arrival of all detection events relative to a trigger event marking the beginning of the experimental sequence. Further processing of the data is done after each experimental run to determine the number of relevant ZPL and readout events. All channels / events that are timing-sensitive (e.g. trigger to the AWG or trigger to the timing board) are generated from a single output event of the FPGA device that triggers the Stanford DG645 signal generators running in burst mode, which have low channel-to-channel and low trigger-to-output jitter.

An additional multi- function DAQ device from NI is used to find and characterize the NVs. It is also used to record a second electronic copy of the photon arrival event on the PSB channel to track the position and frequency drift of the NV/ crysotat/laser system while the entanglement experiment is running.

Finally, we point out that the overall time required for finding and characterizing a low-strain NV is several weeks. Combined with the four day-long data acquisition runs for entanglement verification, the amount of data we are able to take for the same NV becomes limited by the long term stability of our setup. Further improving the robustness of the setup and our ability to locate particular NV's over long time periods will be crucial for future experiments.

2 Level structure and polarization properties of the NV center

In this section we describe the relevant properties of NV centers that allow us to implement the Λ-type entanglement scheme presented in the main text. These properties are rooted in the C_{3v} symmetry of the potential associated with this defect along with spin-spin and spin-orbit interactions in the excited state. They result in an isolated and robust $|A_2\rangle$ state that decays to the $|\pm1\rangle$ states in the ground state triplet through the emission of photons with well defined polarizations along with the $|E_y\rangle$ state that provides a cycling readout transition with the $|0\rangle$ ground state.

2.1 Electronic states of the NV center

The negatively-charged NV defect has six electrons from the nitrogen and the three carbons surrounding the vacancy. They occupy the orbitals a_1', a_1, e_x, e_y whose symmetries are imposed by the nuclear potential. These orbitals transform as the irreducible representations of the C_{3v} group and have been extensively used by many authors[1, 2, 3, 4]. The a_1' and a_1 are lowest in energy and are therefore filled by four of these electrons. The remaining two electrons occupy the degenerate orbitals e_x and e_y. The orbitals e_x and e_y can be viewed as p-type orbitals and $e_+ = -e_x - ie_y$, $e_- = e_x - ie_y$ are analogous to p states with definite orbital angular momentum. Lowest occupation of these orbitals give rise to the triplet ground state

$$|^3A_2\rangle = |E_0\rangle \otimes \begin{cases} |+1\rangle \\ |0\rangle \\ |-1\rangle \end{cases} \tag{1}$$

where $|\pm1\rangle, |0\rangle$ correspond to the $m_s = \pm1, 0$ states, respectively. $|E_0\rangle = |e_xe_y - e_ye_x\rangle$, refers to the orbital state with 0 orbital angular momentum projection along the NV axis. A_2 denotes the orbital symmetry of the state, which is determined by the symmetries of the e_x and e_y orbitals.

The relevant excited state for the optical transitions described in the main text is another pair of triplets which arises from the promotion of one of the electrons occupying the orbital a_1 to the e_x or e_y orbitals [2]. Note that this state can be modeled by one hole in the orbital e and another hole in the orbital a_1, i.e. a triplet in the ae electronic configuration (similarly, the ground state can be modeled by two holes in the e^2 electronic configuration). A total of six states can be formed in this configuration and their symmetries are determined by a group theoretical analysis[5],

$$\begin{aligned}
|A_1\rangle &= |E_-\rangle \otimes |+1\rangle - |E_+\rangle \otimes |-1\rangle \\
|A_2\rangle &= |E_-\rangle \otimes |+1\rangle + |E_+\rangle \otimes |-1\rangle \\
|E_x\rangle &= |X\rangle \otimes |0\rangle \\
|E_y\rangle &= |Y\rangle \otimes |0\rangle \\
|E_1\rangle &= |E_-\rangle \otimes |-1\rangle - |E_+\rangle \otimes |+1\rangle \\
|E_2\rangle &= |E_-\rangle \otimes |-1\rangle + |E_+\rangle \otimes |+1\rangle
\end{aligned} \tag{2}$$

where we have named the first four states as A_1, A_2, E_x and E_y according to their symmetries and named the last two states as E_1 and E_2 since they also transform according to the irreducible representation E. Here, $|E_\pm\rangle = |ae_\pm - e_\pm a\rangle$ and $|X(Y)\rangle = |ae_{x(y)} - e_{x(y)}a\rangle$.

Table S1: Selection rules for optical transitions between the triplet excited state (ae) and the triplet ground state (e^2). Linear polarizations are represented by $\hat{x}$ and $\hat{y}$, while circular polarization are represented by $\hat{\sigma}_\pm = \hat{x} \pm i\hat{y}$. As an example, a photon with σ_+ polarization is emitted when the electron decays from state A_2 to state ${}^3A_{2-}$.

Pol	A_1	A_2	E_1	E_2	E_x	E_y
${}^3A_{2-}$	$\hat{\sigma}_+$	$\hat{\sigma}_+$	$\hat{\sigma}_-$	$\hat{\sigma}_-$		
${}^3A_{20}$					$\hat{y}$	$\hat{x}$
${}^3A_{2+}$	$\hat{\sigma}_-$	$\hat{\sigma}_-$	$\hat{\sigma}_+$	$\hat{\sigma}_+$		

As spin-spin and spin-orbit interactions are invariant under any operation of the C_{3v} group, the states given in equation (2) are eigenstates of the full Hamiltonian including these interactions in the absence of any perturbation such as magnetic field and/or crystal strain. It is known [3, 6] that spin-orbit interaction splits states with different total angular momentum, i.e., the pairs (A_1, A_2), (E_x, E_y) and (E_1, E_2) are split from each other by about 5.5 GHz [7]. The spin-spin interaction also plays a crucial role in the stability of the states $|A_1\rangle$ and $|A_2\rangle$. This interaction shifts up the non-zero spin states (A_1, A_2, E_1 and E_2) by $\sim \frac{1}{3}1.42$ GHz [8, 7] and shift the states $|E_x\rangle$ and $|E_y\rangle$ down by $\sim \frac{2}{3}1.42$ GHz. Thus, the gap between (A_1, A_2) and (E_x, E_y) is increased, but the gap between the states (E_x, E_y) and (E_1, E_2) is reduced. In addition, the spin-spin interaction splits the states $|A_2\rangle$ and $|A_1\rangle$ by ~ 3.3 GHz [7]. Thus, for relatively low strain, we obtain a very robust $|A_2\rangle$ state with stable symmetry properties that are protected by an energy gap arising from the spin-orbit and spin-spin interactions.

2.2 Properties of optical transitions

Once the wavefunctions are known, it is possible to calculate the selection rules of optical transitions between the triplet excited state and the triplet ground state. The dipole moment between the ground and excited state is produced by the hole left in the a orbital under optical excitation. As expected from symmetry arguments, the expectation values of the matrix elements $\langle a|\hat{x}\cdot r|e_x\rangle$ and $\langle a|\hat{y}\cdot r|e_y\rangle$ are non-zero, where $\hat{x}$ and $\hat{y}$ represent the polarization of the involved photon. We can then calculate the selection rules for transitions between every pair of ground and excited states, as shown in Table S1. As expected, these selection rules conserve the total angular momentum of the photon-NV center system.

The allowed optical transitions and their polarization properties indicate several possible Λ schemes in the NV center. However, while these properties are relatively robust in the $|A_1\rangle$ and $|A_2\rangle$ states, the $|A_1\rangle$ state is coupled non-radiatively to a metastable singlet state, which then decays to the ground state $|0\rangle$ and results in leakage out of the ideal Λ system consisting of the $|A_2\rangle$ state and the $|\pm1\rangle$ states. Thus, we find that the $|A_2\rangle$ state provides the most ideal Λ scheme for our present experiment.

2.3 The effect of strain

In order to understand possible imperfections caused by deviations from the ideal case, we now discuss the effect of local strain on the properties of the optical transitions. This perturbation splits the degeneracy between the orbitals e_x and e_y and results in their mixing. In the limit of high strain (larger than the spin-orbit splitting), the excited state manifold splits into two triplets, each with a particular well defined spatial wavefunction. Orbital and spin degrees of freedom separate in this regime and spin-preserving transitions are excited by linearly polarized light. For this reason, it is desirable to work with centers with low strain. An analytic study can be made by considering the following Hamiltonian for the excited state manifold,

$$H = H_{ss} + H_{so} + H_{strain} \quad (3)$$

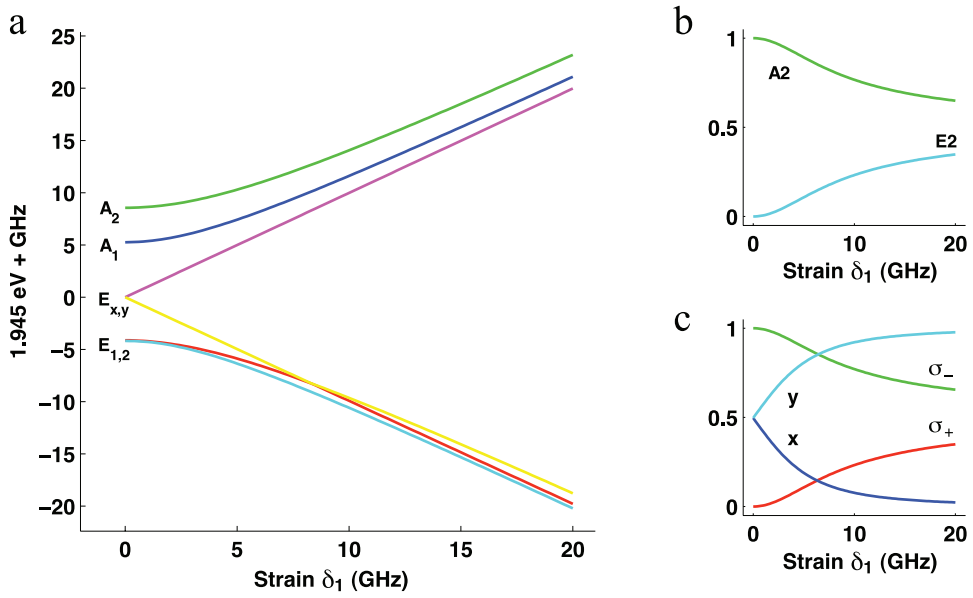

Figure S2: Effect of strain on the properties of the NV center. **a.** Energies of the excited states as a function of strain, expressed in units of the linear strain induced splitting between the $|E_x\rangle$ and $|E_y\rangle$ states. **b.** Strain induced mixing of the $|A_2\rangle$ and $|E_2\rangle$ states, showing the fraction of A_2 and E_2 character of the highest energy excited state. **c.** Polarization character of the optical transition between $|A_2\rangle$ state and the ground state $|+1\rangle$ as a function of strain. As strain increases, the polarization changes from circularly to linearly polarized. The transition between $|A_2\rangle$ and $|-1\rangle$ shows the same behavior, except with σ_- and σ_+ switched. Therefore, at high strain, decay from the $|A_2\rangle$ results in a separable state of the photon polarization and spin rather than an entangled state.

where the spin-orbit and spin-spin [3, 9, 5] Hamiltonians are given by

$$H_{so} = \lambda_z S_z L_z + \lambda_\perp (LS)_\perp \quad (4)$$

$$H_{ss} = \Delta\left(|A_1\rangle\langle A_1| + |A_2\rangle\langle A_2| + |E_1\rangle\langle E_1| + |E_2\rangle\langle E_2|\right) - 2\Delta\left(|E_x\rangle\langle E_x| + |E_y\rangle\langle E_y|\right) + \Delta'\left(|A_2\rangle\langle A_2| - |A_1\rangle\langle A_1|\right) \quad (5)$$

and the strain Hamiltonian is given by [9, 5]

$$H_{strain} = \delta_1\left(|e_x\rangle\langle e_x| - |e_y\rangle\langle e_y|\right) + \delta_2\left(|e_x\rangle\langle e_y| + |e_y\rangle\langle e_x|\right) \quad (6)$$

where $3\Delta \approx 1.42$ GHz and $\Delta' \approx 1.55$ GHz characterize the spin-spin induced zero-field splittings, λ_z is the axial spin-orbit interaction, $\lambda_\perp$ is the non-axial spin-orbit interaction, and δ_1 and δ_2 are different parameters describing the crystal strain. Figure S2 shows an example of how δ_1 strain splits and mixes the excited states, and as a results changes the polarization properties of the optical transitions. A similar effect occurs for δ_2 strain, where $|A_2\rangle$ is mixed with $|E_1\rangle$.

It is worth mentioning that while the excited state configuration is highly affected by strain, the ground state configuration is unaffected to first order due to its antisymmetric combination of e_x and e_y orbitals. It is also protected by the large optical gap between the ground and excited state to second order perturbation in strain.

3 Spin readout

Spin readout is achieved through resonant laser excitation tuned to the $|0\rangle \leftrightarrow |E_y\rangle$ transition[7]. As the $|0\rangle \leftrightarrow |E_y\rangle$ transition is cycling for low strain and is isolated in frequency from other transitions the fluorescence

collected in the presence of the resonant laser field should be proportional to the population in the $|0\rangle$ state. However, the fluorescence levels measured for different spin states may depend on the complex dynamics associated with the singlet state, imperfections of the cycling transition, photoionization, and spatial stability of the measurement setup. In order to accurately calibrate our spin measurements, we use a procedure that involves the conditional preparation of spin states. In the following section, we first describe the conventional spin measurement procedure and then compare it to our conditional readout scheme.

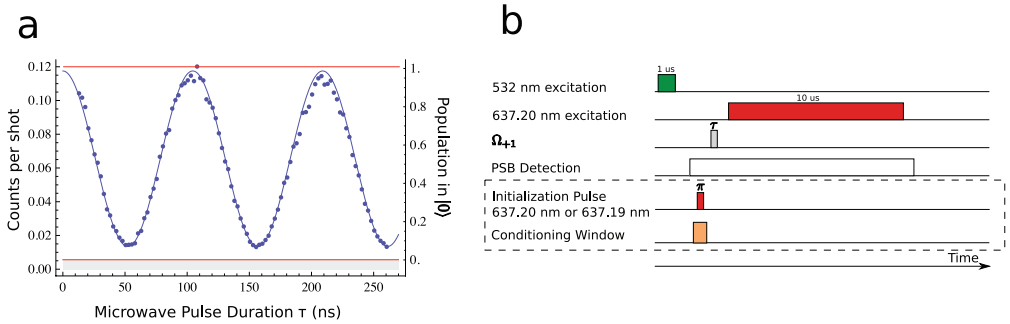

Figure S3: **Spin readout via resonant excitation a** Microwave Rabi oscillations (in blue) recorded using the pulse sequence given in (b) without conditioning. Left vertical axis shows the average number of counts received for a particular length of microwave pulse duration (τ). Right vertical axis shows the normalized population in the $|0\rangle$ state for the same pulse duration. The red lines are maximum and minimum readout levels obtained using the conditioned readout technique shown in (b) and described in the text. **b** Pulse sequence used for part (a). In the unconditioned case, 532 nm light is turned on for 1 μs to polarize the electronic spin to $|0\rangle$ state. After 6 μs, a microwave pulse resonant to the $|0\rangle \leftrightarrow |+1\rangle$ of varying duration is applied. Finally a 10 μs light pulse resonant to the $|0\rangle \leftrightarrow |E_y\rangle$ transition is turned on 1 μs after the microwave pulse and counts in the PSB are recorded in this interval. Additional pulses used for conditioned readout are boxed, including a resonant optical π pulse tuned to the $|0\rangle \leftrightarrow |E_y\rangle$ or $|\pm\rangle \leftrightarrow |A_2\rangle$ transition. Only events where a PSB photon is received within a 20 ns window around this pulse are kept, thus conditioning the readout procedure on a fluorescent decay from the NV.

Figure S3(a) shows microwave Rabi oscillations detected using the conventional resonant readout scheme. Following a polarization step carried out with a green laser, a microwave pulse of varying length and resonant to the $|0\rangle \leftrightarrow |1\rangle$ transition is applied and the resulting state is read out using the resonant excitation. In an ideal preparation and readout scenario, the $|0\rangle$ state would be bright while the $|\pm1\rangle$ states would be completely dark. The high level of fluorescence achieved for the $|0\rangle$ state is limited by the branching ratio between the $|E_y\rangle \rightarrow |0\rangle$ and $|E_y\rangle \rightarrow |\pm1\rangle$ transitions ($\sim$99 % as measured below) and the collection efficiency to about 0.11 counts per shot. Thus multiple repetitions of the experiment are needed to build up enough statistics for an accurate estimation of the initial state. When the NV center is nominally prepared in the $|+1\rangle$ state, we observe counts above the background level, which may be due to imperfect spin polarization or additional fluorescence from the $|+1\rangle$ state.

To characterize these effects further, we record time traces of the fluorescence during the resonant readout stage where the state is initialized either in $|0\rangle$ or $|1\rangle$ in the same way as the Rabi experiment (Figure S4(b)). These are then compared to a model of the NV center dynamics similar to the one discussed in [6] and illustrated in Figure S4(c). The model involves the $|0\rangle$ and $|\pm1\rangle$ ground states, the $|E_y\rangle$ state, and a metastable singlet state $|S\rangle$. The branching ratios from $|E_y\rangle$ state to $|0\rangle$, $|\pm\rangle$, and $|S\rangle$ are related to the decay rates $\gamma_{00} = 1/12$ns, γ_{01}, and γ_{0s}, respectively. γ_{00} is determined by lifetime measurements, and the singlet decay rate to $|0\rangle$ is set to $\gamma_s = \gamma_{00}/33$, as given in [6]. We then simulate the evolution of the system under a continuous optical pumping of the $|0\rangle \rightarrow |E_y\rangle$ transition at a rate R, starting with some initial spin population for the two cases of initialization in $|0\rangle$ or $|1\rangle$. To estimate the values of γ_{01}, γ_{0s}, R, and the spin polarization, these parameters are varied to fit the simulation to the data by eye. This was done for

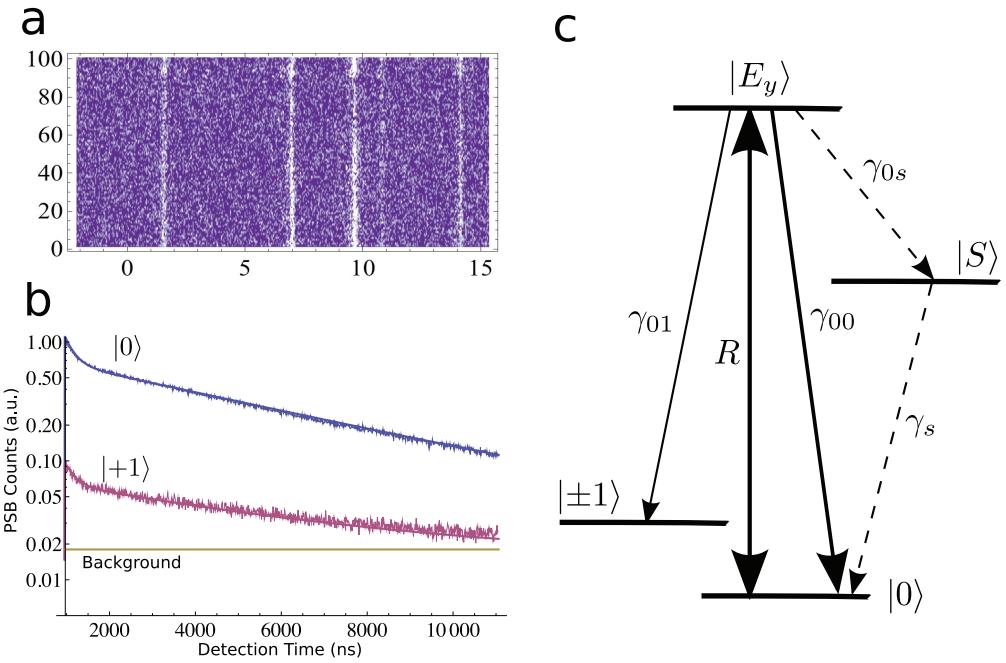

Figure S4: **Stability and dynamics of optical transitions a** One hundred successive scans of the NV spectrum shown in Figure 2(b) of the main text. Each scan taken over ∼10 seconds, demonstrating the spectral stability of the NV center over long time scales. Spectral lines shown here and in Figure 2b of the main text have widths larger than 100 MHz due to power broadening. **b** Histograms showing time traces of fluorescence as recorded in the PSB following spin initialization to either the $|0\rangle$ (red) or $|1\rangle$ (blue) state. Solid lines show simulated fluorescence from the NV using the model shown in (c) and described in the text. Two other similar data sets at different laser powers were used to determine the branching ratio of $|E_y\rangle$ to $|\pm1\rangle$ and the spin polarization. **c** Model used to simulate the dynamics of optical transitions leading to fluorescence time traces shown in (b). R gives the optical pumping rate of the readout transition. γ_{00} and γ_{01} are decay rates to the $|0\rangle$ and $|\pm1\rangle$ states, respectively. γ_{0s} and γs are the non-radiative decay rates into and out of the metastable singlet state $|S\rangle$.

three different laser powers, and the data and simulation results for the medium power are shown in Figure S4(b), which corresponds to conditions under which the Rabi curve in Figure S3(a) where taken. Using this method, we estimate the branching ratio out of the system of $m_s = 0$ states to be $0.92 \pm 0.16\%$, and the imperfection in spin preparation to be $7.2 \pm 1.8\%$. This imperfection could be either due to incomplete spin polarization or imperfect microwave pulses. The pulse error associated with a square pulse of finite Rabi frequency (around 10 MHz) is estimated to be about 3 %. The error is mostly due to the presence of the hyperfine interaction with the nuclear spin of ^{14}N associated with the NV center[10]. We thus estimate the spin polarization after the green excitation to be $96 \pm 1.9\%$.

To directly calibrate our spin readout results and confirm that it is the imperfect spin preparation stage which reduces the contrast of the Rabi experiment, we perform two experiments in which we polarize the NV center by measurement and perform conditional spin readout. In the first experiment, a π pulse (initialization pulse) resonant to the $|0\rangle \leftrightarrow |E_y\rangle$ transition is applied many lifetimes prior to microwave manipulation. By only analyzing events in which a photon has been detected in the PSB during the initialization pulse, we ensure that a photon has decayed from the $|E_y\rangle$ state prior to microwave manipulation. The state should decay to the $|0\rangle$ state with 99 % probability, and given that the signal / noise of the trigger photon is roughly 280:1, the state should be prepared in $|0\rangle$ with 99 % probability prior to microwave pulses. Subsequent

measurement of the spin by a separate laser tuned to the same transition reveals 0.13 ± 0.025 counts /shot if no microwave manipulation is carried out and 0.0092 ± 0.00054 counts/shot if a microwave π pulse is applied resonant to the $|0\rangle \leftrightarrow |+1\rangle$ transition. The ratio of the counts after subtracting the background of 0.0057 ± 0.0010 counts/shot is accounted for by the expected pulse error. A second experiment was carried out where the initialization pulse was tuned resonant to the $|+1\rangle \leftrightarrow |A_2\rangle$ transition. The detection of a photon in the PSB indicates that the state has been prepared in the $|\pm 1\rangle$ manifold, and a subsequent readout process without any microwave manipulation yields the background level. We then conditionally measure the populations in the $|\pm 1\rangle$ states by individually transferring their population back to $|0\rangle$ state. We find that their population levels are roughly equal (0.059 ± 0.0013 counts/shot and 0.061 ± 0.0014 counts/shot). Assuming that the PSB emission does not change the spin projection, this data indicates that the $|A_2\rangle$ state decays with roughly equal probability to $|\pm 1\rangle$ states.

We note that the readout levels achieved by the conditioned measurement procedure could in principle be different from the values obtained without conditioning. Although the difference is small for the NV center used in the current experiment, we have observed a significant difference for other NV centers. One possible source for this difference is photoionization of the NV^- to NV^0, in which case the center effectively goes dark. The detection of a PSB photon during the conditional calibration procedure described above ensures that the center is in the NV^- state for that particular repetition of the experiment. The readout levels obtained using this procedure are then relevant for normalization of our entanglement verification data, which are similarly conditioned on the detection of a ZPL photon. On the other hand, if no such conditioning was performed, the calibration levels obtained would be reduced by the probability of ionizing the NV, and would not accurately correspond to our entanglement data. In addition, there are many other sources of noise that would have a similar effect, for example spectral instabilities of the laser - NV center system and mechanical vibrations that quickly misalign the system. These effects are slow compared to the repetition rate of our experiment, but short compared to the total data acquisition time and could generate a difference in the two spin readout methods. The NV center we work with has good long term spectral stability within a linewidth of $\sim$100 MHz (Figure S4(a)), and we actively track the position of the NV by maximizing the fluorescence counts during the experiment. However, to completely eliminate the effect of possible instabilities, we normalize our measurements to the conditional calibration values. The population P in state $|0\rangle$ for a given number of counts per repetition (C) is then $P = (C - c_B) / (C_M - c_B)$, where $c_B = 0.0057 \pm 0.0010$ counts/shot and $c_M = 0.11 \pm 0.0022$ counts / shot correspond to the background and maximum calibration values, respectively.

In summary, we find that resonant excitation in combination with conditioning-based spin preparation is an exceptionally useful tool for spin readout of the NV center. Not only can we use it to extract information about populations in relatively few repetitions, but it allows us to fully characterize various procedures related to the spin properties of the NV center, for example spin polarization achieved or pulse errors, with very few assumptions. In addition, the conditioned readout technique may be useful in probing other properties of the NV center such as blinking and spectral stability.

4 Verification of polarization selection rules for $|A_2\rangle$ state

Figure 2c in the main text verifies that transitions from $|\pm 1\rangle$ states to the $|A_2\rangle$ state have mutually orthogonal circular polarizations. Here we explain the observation shown in the figure and describe how we can extract the polarization imperfections of our system.

To obtain Figure 2c, the NV center is prepared in the $|+1\rangle$ ($|-1\rangle$) state with a 1 μs polarization step of off-resonant green excitation followed by a microwave π pulse resonant to the $|0\rangle \leftrightarrow |+1\rangle$ ($|0\rangle \leftrightarrow |-1\rangle$) transition. This transfer of population is followed by a short (2 ns) resonant optical excitation pulse tuned to the $|+1\rangle \leftrightarrow |A_2\rangle$ ($|-1\rangle \leftrightarrow |A_2\rangle$) transition. The fluorescence intensity recorded in the PSB in the presence of this excitation pulse is plotted as function of quarter wave plate (QWP) angle. The wave plate rotates the incident linearly polarized light into a well defined superposition of circular polarizations dependent on the angle. The length and intensity of the pulse is chosen such that it is close to an optical π pulse for the appropriate QWP angle that maximizes the fluorescence for the selected transition.

The electric field projections to σ_+ and σ_- after the linearly polarized excitation beam passes the QWP at an angle θ are $\frac{1}{2}\left(i+e^{-2i\theta}\right)$ for σ_+ and $\frac{1}{2}\left(i+e^{2i\theta}\right)$ for σ_-, so that the intensities in σ_+ and σ_- oscillate out of phase as functions of 2θ.

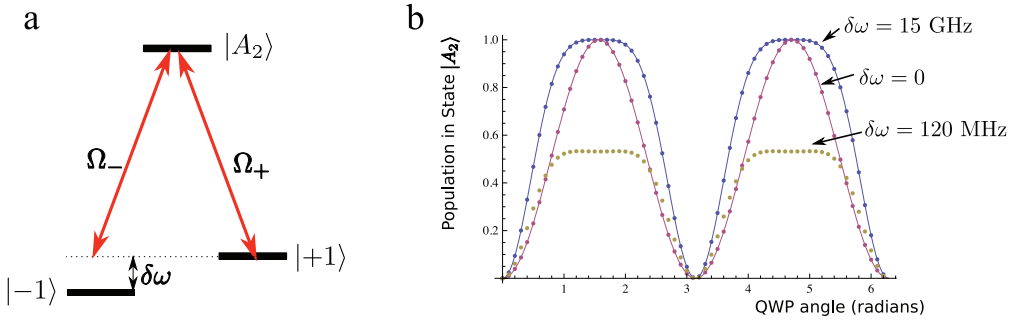

Figure S5: Model and simulations for verification of circular polarization. **a** Simplified model used to explain the non-sinusoidal behavior. The excited state $|A_2\rangle$ is coupled to the ground states $|\pm1\rangle$ with optical Rabi frequency $\Omega_\pm$. These Rabi frequencies are determined by the particular QWP angle θ. The state prepared with microwave excitation is on-resonance with the optical field while the other is detuned by $\delta\omega$ in the presence of the Zeeman splitting ($2\pi \times 120$ MHz). **b** Calculated excited state populations for $\Omega = \sqrt{\Omega_+^2 + \Omega_-^2} = 2\pi \times 250$ MHz. The pulse is on for 2 ns for the blue and red dots and 3.5 ns for the yellow dots. The detuning is assumed to be 0 for the red dots, 15 GHz for the blue dots and 120 MHz for the yellow dots. Solid lines are plots of expressions for the population in the two limits explained in the text.

Dynamics of the NV center under excitation by polarized light may be extracted from the simple model shown in Figure S5. As our excitation beam is tuned to a particular transition, say $|+1\rangle \leftrightarrow |A_2\rangle$, the other transition from $|-1\rangle$ is detuned by the Zeeman splitting $\delta\omega$. The optical Rabi frequencies associated with each transition are QWP angle dependent: $\Omega_+ = \frac{\Omega}{2}\left(i+e^{-2i\theta}\right)$ and $\Omega_- = \frac{\Omega}{2}\left(i+e^{2i\theta}\right)$. We neglect spontaneous decay for simplicity since the optical excitation is relatively short. Our measured signal then corresponds to the population in the $|A_2\rangle$ state after 2 ns ($t = \pi/\Omega$) of evolution under optical excitation from the initial $|+1\rangle$ or $|-1\rangle$ state.

We first consider the limit $\Omega \gg \delta\omega$, where the natural basis is the "bright" and "dark" states defined by $|b\rangle = \frac{\Omega_+|+1\rangle + \Omega_-|-1\rangle}{\Omega}$ and $|d\rangle = \frac{\Omega_+|+1\rangle - \Omega_-|-1\rangle}{\Omega}$. The applied excitation always acts as an optical π pulse that transfers the population from $|b\rangle$ to $|A_2\rangle$. As the QWP rotates, our signal varies with the overlap between the prepared state $|\pm1\rangle$ and the bright state: $|\langle\pm1|b\rangle|^2 = \frac{1\pm\sin 2\theta}{2}$. The expected angular dependence is sinusoidal, as demonstrated in Figure S5

In the opposite limit where $\Omega \ll \delta\omega$, the detuned state is mostly off resonant, and the natural basis is again $|+1\rangle$ and $|-1\rangle$. In this case we may neglect the off resonant level and consider two-level Rabi oscillations between the prepared state and $|A_2\rangle$. The population in the excited state for this case is given by $\sin^2\left(\Omega_\pm t/2\right) = \sin^2\left(\frac{\pi\sqrt{(1\pm\sin 2\theta)}}{2\sqrt{2}}\right)$. As illustrated in Figure S5, the population curve has a flattened top compared to a simple sinusoid.

For the NV center considered in the main text, $\Omega \sim 2\pi \times 250$ MHz and $\delta\omega \sim 2\pi \times 122$ MHz. We are thus in the intermediate regime between the two limits. As the QWP is rotated, both the Rabi frequency and the overlap with the bright state change, leading to more complex behavior. The yellow dots in Figure S5b shows that if t is picked to be slightly longer than a π pulse, the $|A_2\rangle$ population is nearly independent of angle near circular polarization. As the angle deviates from the $\theta = \pi/2$, the Rabi frequency decreases so that the population transferred to the $|A_2\rangle$ state increases. On the other hand, the overlap of the prepared state with the bright state decreases. The combination of these two effects give rise to an extended flat-top behavior.

In addition, Figure 2c in the main text shows that the $|+1\rangle$ and $|-1\rangle$ cases give rise to differently shaped curves. We attribute this to different overlap of the confocal spot with the NV for the two measurements, which also explains the slightly different collection efficiencies assumed for the two cases to fit the observed data. The fits used in the figure also include decay from the excited state, which decreases the population transfered to the excited state, but has no other significant effect.

The finite contrast observed in Figure 2c could be due to imperfect selection rules between the $|A_2\rangle$ and ground states or imperfect circular polarization of the optical excitation. With Figure 2c alone it is not possible to distinguish between the two cases. Given the above discussion of the excited states, we estimate the mixing between the $|A_2\rangle$ states and other excited states to be about 1 %. From these considerations we deduce that that the selection rules are nearly perfect as described before, but that the imperfect optical system creates a slightly elliptical electric field vector $0.94|\sigma_+\rangle + 0.34|\sigma_-\rangle$. This ellipticity is expected to decrease the observed fidelity by 12 %.

5 Effects of magnetic environment, detunings, and echo

The entangled state given in Eq. 1 of the main text is suceptable to fluctuations from the magnetic enviroment. In this section we show that these fluctations and unaccounted detunings between the microwave fields and NV center transitions would lead to a decreased contrast of the observed oscillations. We then describe the echo technique used to improve the contrast.

We note that these imperfections, in the current context, mainly affect measurements in the H, V basis. Their effect on the $\sigma_\pm$ basis is limited to inefficiencies in population transfer to $|0\rangle$ state and are thus accounted for by pulse errors, which are treated seperately.

5.1 Effect of Finite Detuning

We generalize the description given in the main text by introducing the rotating frame associated with the microwave fields:

$$|\pm\tilde{1}\rangle_t = e^{i\phi_\pm} e^{-i(\omega_\pm \mp \Delta)t} |\pm 1\rangle,$$

where we have added a particular detuning Δ that covers the effect of hyperfine coupling to ^{14}N nuclear spin and AC Stark shifts from non-resonant microwave fields. For the NV center used in this study there are no nearby ^{13}C nuclear spins, hence their effect may be neglected. We estimate the static detuning of our microwave field from the relavent NV transtion frequencies to be less then 500 kHz. The two microwave frequencies are well separated by $\delta \sim 120$ MHz, so the presence of the non-resonant field mainly creates an AC Stark shift. For our Rabi frequency of 8 MHz the shift is estimated to be $\Omega^2/\delta \sim 0.5$ MHz. For the idling times considered (~ 500 ns), the effect of the ^{13}C nuclear bath is relatively small.

Under these assumptions, the state right before detection of the photon may then be written as:

$$|\Psi(t_d)\rangle = \frac{1}{\sqrt{2}} \left(e^{-i\phi_+} e^{i(\omega_+ - \Delta)t_d} |\sigma_+\rangle |-\tilde{1}\rangle_{t_d} + e^{-i\phi_-} e^{i(\omega_- + \Delta)t_d} |\sigma_-\rangle |+\tilde{1}\rangle_{t_d} \right).$$

Following the detection and idling time t_i, the state becomes:

$$|\Psi(t_d)\rangle_{t_i} = \frac{1}{\sqrt{2}} \left(e^{-i\phi_+} e^{i(\omega_+ - \Delta)t_d - \Delta t_i} |-\tilde{1}\rangle_{t_i} \pm e^{-i\phi_-} e^{i(\omega_- + \Delta)t_d + \Delta t_i} |+\tilde{1}\rangle_{t_i} \right)$$

where $+$ $(-)$ corresponds to detection of a photon in H (V) states. The idling time effects the signal we observe through (re-defining α from the main text):

$$\alpha = (\omega_+ - \omega_- - 2\Delta)t_d + 2\Delta t_i - \Delta\phi$$

For example, the presence of ^{14}N nuclear spin introduces a fixed detuning that is static for the duration of an experimental run, but from run to run changes between $\Delta = 0, \pm 2.2$ MHz [10]. For t_i of order 200 ns

the detuning may decrease the observed contrast significantly. While this effect can be reduced by simply waiting for an appropriate rephasing time for the ^{14}N, there is still residual decoherence due to the ^{13}C spin bath. To best eliminate all these effects and extend the memory time of the spin state, we add an echo sequence prior to spin measurement.

5.2 Spin Echo Sequence

The echo is easiest to describe in the $|M\rangle = \left(|+\tilde{1}\rangle + |-\tilde{1}\rangle\right)/\sqrt{2}$ and $|D\rangle = \left(|+\tilde{1}\rangle - |-\tilde{1}\rangle\right)/\sqrt{2}$ basis. We apply a $t_i - 2\pi - t_i$ sequence with microwave pulses that drive the $|M\rangle \leftrightarrow |0\rangle$ transition. This sequence is in spirit similar to the Bang-Bang decoupling technique[11]. For an arbitrary superposition $|\psi\rangle$ of the orthogonal states $|M\rangle$ and $|D\rangle$, evolution of time t_i under the detuning of the form given above leads to coherent oscillations between the states $|D\rangle$ and $|M\rangle$ and results in the state $e^{-i2\Delta t_i \sigma_x}|\psi\rangle$, where σ_i is the appropriate Pauli matrix in the $|M\rangle$, $|D\rangle$ basis. If the magnetic field fluctuates from shot to shot this leads to decoherence. A fast 2π pulse effectively switches the sign of the $|M\rangle$ state ($\sigma_z e^{-i2\Delta t_i \sigma_x}|\psi\rangle$). The subsequent evolution then creates the state $e^{-i2\Delta t_i \sigma_x}\sigma_z e^{-i2\Delta t_i \sigma_x}|\psi\rangle = \sigma_z|\psi\rangle$, which differs from the original state only by a relative phase that is independent of Δt_i.

In the context of section S.4.1, the procedure above results in the following state after the echo sequence in the $|\pm\tilde{1}\rangle$ basis: $\frac{1}{\sqrt{2}}\left(e^{-i\phi_+}e^{i(\omega_+ - \Delta)t_d}|-\tilde{1}\rangle \pm e^{i\phi_-}e^{i(\omega_- + \Delta)t_d}|-\tilde{1}\rangle\right)$. Hence our signal is only affected by the random arrival time of the photon t_d and not the idling time. For detunings on the order of 5 MHz, the frequency shift is about 4 % of the center frequency of the oscillations (120 MHz) and may be neglected within our current signal to noise.

We note that for a finite length of the 2π pulse (around 110 ns), the echo is expected to be imperfect, as the magnetic field continues to rotate the states in the $|M\rangle$, $|D\rangle$ basis while the pulse is being applied. By timing the echo sequence correctly, we can compensate for this imperfection.

To find the optimal timing of t_i for our experiment, we carry out a simple echo experiment illustrated in Figure S6. Given Figure S6b we pick $t_i = 170$ ns for optimum compensation such that an almost perfect echo is performed.

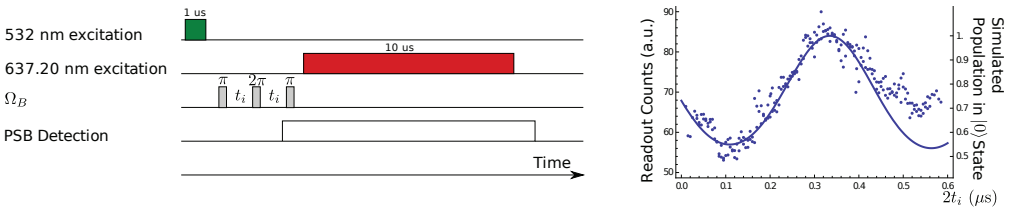

Figure S6: Echo technique used. **a**. Pulse sequence implemented to test the echo technique. The system is initialized to the $|0\rangle$ state followed by 5 μs of waiting time. A π pulse is applied to create a bright superposition $|M\rangle$ of $|\pm 1\rangle$ states. The state is allowed to evolve for time t_i before a 2π refocusing pulse is applied, after which the state evolves for time t_i again. A π pulse then maps the state back to $|0\rangle$ and is followed by a resonant readout pulse. **b**. Result of the sequence described in part (a). Solid line is a theory fit where only the effect of ^{14}N has been taken into account.

6 Fidelity estimates

We would like to determine the lower bound for the entanglement fidelity[12]:

$$F \geq (F_1 + F_2)/2 \tag{7}$$

where

$$F_1 = \rho_{\sigma_+ -1,\sigma_+ -1} + \rho_{\sigma_- +1,\sigma_- +1} - 2\sqrt{\rho_{\sigma_+ +1,\sigma_+ +1}\rho_{\sigma_- -1,\sigma_- -1}} \tag{8}$$

$$F_2 \quad = \quad \rho_{H+,H+} - \rho_{H-,H-} + \rho_{V-,V-} - \rho_{V+,V+}. \tag{9}$$

We obtain $F_1 = 0.83 \pm 0.10$ by measuring the quantities $\rho_{\sigma_+ -1,\sigma_+ -1}$, $\rho_{\sigma_- +1,\sigma_- +1}$, $\rho_{\sigma_+ +1,\sigma_+ +1}$, and $\rho_{\sigma_- -1,\sigma_- -1}$ in the original basis of the photon and spin. F_2 is related to the oscillation amplitudes $a_H/2 = \rho_{H-,H-} - \rho_{H+,H+}$ and $a_V/2 = \rho_{V+,V+} - \rho_{V-,V-}$, measured in the rotated basis.

6.1 Time bin optimization

One approach to obtaining the amplitudes a_H and a_V is by directly fitting to the oscillations in the conditional probability, as shown in Figure 4c of the main text. The resolution of our time-tagged-single-photon-counting device is 4 ps. However, due to our low count rates, only a fraction of the 4 ps time bins register a photon in the signal region during the entire experimental run. Therefore, to obtain the conditional probability, we group the ZPL counts and their corresponding readout results into larger time bins. One commonly used method is to optimize the goodness of the fit of a particular model to the data by varying size of the bins so that the error of the fit is minimized[13] . However, such a method involves computationally intensive procedures. Therefore we have used a simplified version of this method, motivated by the fact that our count rates decrease exponentially as a function of t_d. In essence, the time bins are determined one at a time starting from the beginning of the decay by minimizing the fit error while varying each successive time bin between 900 ps and 2 ns, which is longer than the timing resolution of our photon detectors (~ 300 ps) and shorter than the period of the expected oscillations. Since the count rate is highest at the beginning of the decay and should therefore be amenable to the smallest time bins, we start by fixing the first three time bins to 900 ps. We then add the next time bin, vary its length, and perform a fit to the data in these first four bins. The length of the fourth bin is then chosen to minimize the mean squared error of the fit. This optimization process is repeated for each successive time bin until 15 ns of data are used. Such an optimization of the bin sizes is done separately for the H and V polarizations.

We emphasize that the time bins are chosen to optimize the error of the resulting fits, not the amplitude of the fitted oscillations. As shown in Figure 4c, the time-binned data exhibit clear oscillations and allows us to extract a fidelity above the classical limit using the fit.

6.2 Maximum Likelihood Estimate

Any time binning method, while necessary to present the data in a reasonable fashion, introduces errors by changing the timing information of the raw data. In order to ensure that such errors do not lead to an incorrect estimate of the fidelity, we also extract the fidelity directly from the raw data using a maximum likelihood method. In addition, we calculate the probability distribution for the fidelity, which not only indicates a high probability of entanglement demonstration, but, by virtue of being nearly a perfect Gaussian, justifies minimization of the mean squared error used in the optimization procedure above.

We first derive the formula for the joint probability distribution function of detecting a photon at time t and measuring the spin state $|M\rangle$. Due to the single exponential decay of the optical excited state, the probability distribution for detection of a $|H\rangle$ or $|V\rangle$ photon at time t is

$$p_{H,V}(t) = \frac{1}{\tau} e^{-t/\tau}, \tag{10}$$

where $\tau = 12$ ns is the lifetime of the excited states. For a perfect spin-photon entangled state, upon detection of a $|H\rangle$ or $|V\rangle$ photon at time t, the conditional probability of measuring the spin state $|M\rangle$ is $p_{M|H,V}(t) = \frac{1}{2}(1 \pm \cos\alpha(t))$ with $\alpha(t) = (\omega_+ - \omega_-)\, t + (\phi_+ - \phi_-)$. For an imperfect spin photon entangled state, the conditional probability has a reduced oscillation amplitude:

$$p_{M|H,V}(t) = \frac{1}{2}(1 \pm a_{H,V} \cos\alpha(t)). \tag{11}$$

Thus, the joint probability is

$$p_{M;H,V}(t) \quad = \quad p_{M|H,V}(t)\, p_{H,V}(t) \tag{12}$$

$$= \frac{1}{2\tau} e^{-t/\tau} \left(1 \pm a_{H,V} \cos\alpha\left(t\right)\right). \tag{13}$$

Motivated by these considerations we aim to model the experimental data using the following fitting functions:

$$f_H\left(t\right) = \frac{c_H}{2}\left(1 + a_H \cos\left(2\pi t/T + \phi\right)\right) e^{-t/\tau} + b_0, \tag{14}$$

$$f_V\left(t\right) = \frac{c_V}{2}\left(1 - a_V \cos\left(2\pi t/T + \phi\right)\right) e^{-t/\tau} + b_0, \tag{15}$$

with fitting parameters $\{c_H, c_V, a_H, a_V, T, \phi, b_0\}$. Here c_H and c_V are proportional to duration of the experiment and b_0 is the background.

We denote the number of conditional readout events within each $\Delta t = 4$ ps detection time bin $[t, t+\Delta t]$ as $n_{H,t}$ and $n_{V,t}$ for the two photon polarizations, and obtain the data sets $\{n_{H,t}\}$ and $\{n_{V,t}\}$ with $t = t_0, t_0 + \Delta t, t + 2\Delta t, \cdots$. For a given set of data and underlying probability model, a maximum likelihood estimate (MLE) picks the values of the model parameters that maximize the *likelihood function* for the data, compared to other choices of parameters. Given no prior knowledge of the fitting parameters, we may assume an uniform distribution for the fitting parameters. Then the likelihood function will be proportional to the probability distribution function. In the following, we use the MLE to fit the theoretical model with experimental data and obtain the oscillation amplitudes a_H and a_V.

The expected average number of events for the time bin $[t, t+\Delta t]$ are given by equations 14 & 15 above. However, the number of recorded events for each time bin has fluctuations characterized by the Poisson distribution

$$p_\lambda\left(n\right) = \frac{\lambda^n}{n!} e^{-\lambda}, \tag{16}$$

where λ is the average number of events. Thus, the *likelihood* for recording $n_{H,t}$ events of detecting an $|H\rangle$ photon at time t and measuring the NV center in spin state $|M\rangle$ is

$$L_H\left(n_{H,t}, t\right) = p_\lambda\left(n_{H,t}\right)|_{\lambda = f_H(t)} \tag{17}$$

$$= \frac{f_H(t)^{n_{H,t}}}{n_{H,t}!} e^{-f_H(t)}. \tag{18}$$

The likelihood for getting the list $\{n_{H,t}\}$ is

$$L_H\left(\{n_{H,t}\}\right) = \prod_t L_H\left(n_{H,t}, t\right). \tag{19}$$

Similarly, the likelihood for the list $\{n_{V,t}\}$ is

$$L_V\left(\{n_{V,t}\}\right) = \prod_t L_V\left(n_{V,t}, t\right), \tag{20}$$

where

$$L_V\left(n_{V,t}, t\right) = \frac{f_V\left(t\right)^{n_{V,t}}}{n_{V,t}!} e^{-f_V(t)}. \tag{21}$$

We numerically maximize the following likelihood function for both lists $\{n_{H,t}\}$ and $\{n_{V,t}\}$:

$$L\left(\{n_{H,t}\}, \{n_{V,t}\}\right) = L_H\left(\{n_{H,t}\}\right) L_V\left(\{n_{V,t}\}\right). \tag{22}$$

We use the generic gradient ascend algorithm to maximize the likelihood function with the optimal choice of parameters as listed in Table S2. We verify that it is also a global maximum by sampling throughout the entire parameter space numerically.

In Figure S7a, we plot the contour of likelihood as a function of a_H and a_V. Since we have no prior knowledge about the parameters a_H and a_V, we can use an uniform prior probability distribution for a_H

Parameter	a_H	a_V	c_H	c_V	T (ns)	ϕ	b_0
value	0.65	0.55	0.083	0.090	8.2	−4.04	0.000

Table S2: Optimal choice of parameters from the MLE.

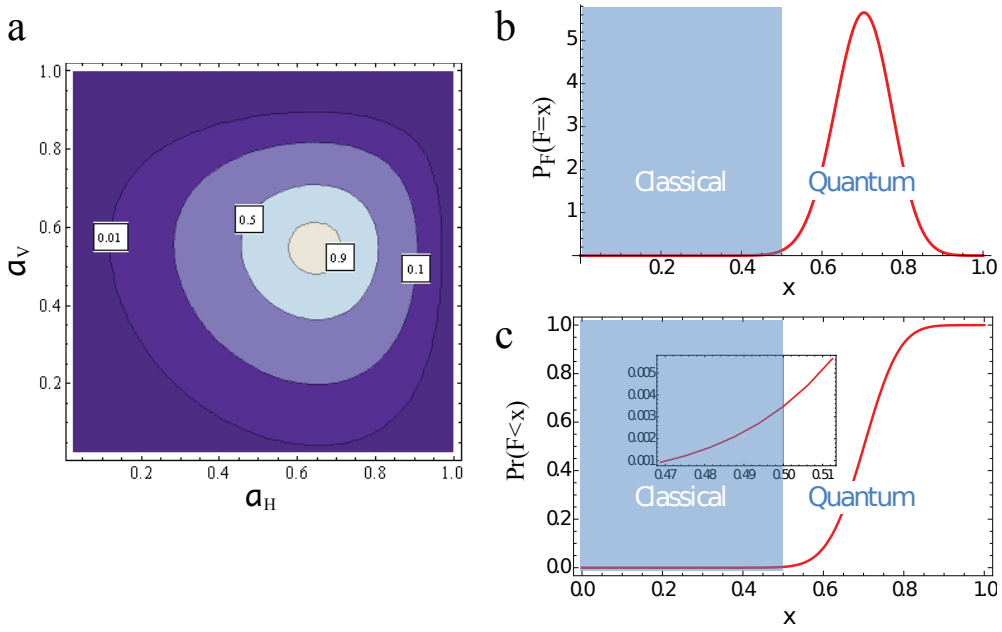

Figure S7: Results of maximum likelihood estimate. **a.** Contour plot of likelihood as a function of a_H and a_V. The contour lines represent relative likelihood of 90%, 50%, 10%, 1% from inside out. With no prior knowledge of a_H and a_V, the likelihood is proportional to the probability distribution. **b.** The probability distribution for the lower bound on the entanglement fidelity F. **c.** The cumulative probability distribution for the entanglement fidelity F. Inset: A zoomed plot around $F = 0.5$, showing the cumulative probability is only 0.35%.

and a_V. Then the 2D likelihood plot is proportional to the 2D probability distribution P_{a_H,a_V} joint with the observed data.

The marginal probability distribution $P_{a_H+a_V}$ associated with $a_H + a_V$ is the projection of the full distribution to the +45° direction. The marginal probability distribution can be obtained by integrating the 2D probability P_{a_H,a_V} along the −45° direction:

$$P_{a_H+a_V}(u) \propto \int dv P_{a_H,a_V}\left(\frac{u+v}{2}, \frac{u-v}{2}\right). \tag{23}$$

Because $F_2 = (a_H + a_V)/2$, we obtain the probability distribution for F_2:

$$P_{F_2}(x_1) \propto P_{a_H+a_V}(2x_1). \tag{24}$$

The probability distribution for the lower bound on the fidelity is a convolution of $P_{F_1}(x)$ and $P_{F_2}(x)$:

$$P_F(F = x) = \int_{-\infty}^{+\infty} dx_1 P_{F_1}(x_1) P_{F_2}(x - x_1), \tag{25}$$

where P_{F_1} is assumed to be a Gaussian probability distribution for F_1 with mean 0.83 and standard deviation 0.10. We find that the distribution $P_F(x)$ in Figure S7b is nearly Gaussian and obtain an entanglement

fidelity of $F \geq 0.70 \pm 0.070$. The cumulative probability distribution

$$\Pr(F < x) = \int_{-\infty}^{x} dx' P_F(x') \tag{26}$$

is shown in Figure S7c and indicates that the probability that the entanglement fidelity is above the quantum threshold of 0.5 is

$$\Pr(F > 0.5) = 99.7\%. \tag{27}$$

These results confirm that our experiment provides a reliable observation of spin-photon entanglement.

References

[1] Loubser, J. and Van Wyk, J., Electron spin resonance in the study of diamond. *Rep. Prog. Phys.* **91**, 1201 (1978).

[2] Goss, J., Jones, R., Breuer, S., Briddon, P., and Oberg, S., The twelve-line 1.682 ev luminescence center in diamond and the vacancy-silicon complex. *Phys. Rev. Lett.* **77**, 3041 (1996).

[3] Lenef, A. and Rand, S., Electronic structure of the nv center in diamond: Theory. *Phys. Rev. B* **53**, 13441 (1996).

[4] Gali, A., Fyta, M., and Kaxiras, E., Ab initio supercell calculations on nitrogen-vacancy center in diamond: Electronic structure and hyperfine tensors. *Phys. Rev. B* , 155206 (2008).

[5] Maze, J., Gali, A., Togan, E., Chu, Y., Trifonov, A., *et al.* Group theory of defects: nitrogen-vacancy center. *In preparation* (2010).

[6] Manson, N., Harrison, J., and Sellars, M., Nitrogen-vacancy center in diamond: Model of the electronic structure and associated dynamics. *Phys. Rev. B* **74**, 104303 (2006).

[7] Batalov, A., Jacques, V., Kaiser, F., Siyushev, P., Neumann, P., *et al.* Low temperature studies of the excited-state structure of negatively charged nitrogen-vacancy color center in diamond. *Phys. Rev. Lett.* **102**, 195506 (2009).

[8] Fuchs, G.D., Dobrovitski, V. V., Hanson, R., Batra, A., Weis, C. D., *et al.* Excited-state spectroscopy using single spin manipulation in diamond. *Phys. Rev. Lett.* **101**, 117601 (2008).

[9] Rogers, L., McMurtrie, R., Sellars, M., and Manson, N. B., Time-averaging within the excited state of the nitrogen-vacancy centre in diamond. *New Journal of Physics* **11**, 063007 (2009).

[10] Jelezko, F., Wrachtrup J., Quantum information processing in diamond. *J. Phys.: Condens. Matter*, **18**, S807-824 (2006).

[11] Morton, J. J. L., Tyryshkin, A. M., Ardavan, A., Benjamin, S. C., Porfyrakis, K., *et al.* Bang-bang control of fullerene qubits using ultrafast phase gates. *Nature Physics*, **2**, 40, (2006).

[12] Blinov, B. B., Moehring, D. L., Duan, L. M., Monroe, C., Observation of entanglement between a single trapped atom and a single photon. *Nature* **428**, 153-15 (2004).

[13] Kanazawa, Y., An optimal variable cell histogram based on the sample spacings. *The Annals of Statistics*, **20**, 291-304, (1992).